PCCP

PAPER

View Article Online
View Journal | View Issue



Cite this: *Phys. Chem. Chem. Phys.*, 2024, **26**, 16191

# Thermal behaviors during lithium diffusion in $Li_{0.4}WO_3$ bronze studied by elastic and quasi-elastic neutron scattering†

M. Mangir Murshed, *[ad] Michael Fischer, [bd] Michael M. Koza [c] and Th. M. Gesing [ad]

Received 21st February 2024,
Accepted 20th May 2024

DOI: 10.1039/d4cp00752b

rsc.li/pccp

Polycrystalline $Li_{0.4}WO_3$ bronze has been synthesized by solid state reaction carried out in a silica tube at $10^{-7}$ MPa and 973 K. The sample is characterized by temperature-dependent neutron elastic and quasielastic scatterings. The room-temperature neutron powder data Rietveld refinement confirmed the space group $Im\bar{3}$ along with lithium occupancy found predominantly at the 6*b* crystallographic site. Upon increasing temperature above 300 K lithium at 6*b* site decreases and at 2*a* site increases, suggesting $Li^+$ cation diffusion between these two sites demonstrated by quasielastic neutron scattering as well. The lattice thermal expansion anomaly is observed between 380 K and 450 K, which is explained in terms of lithium dynamic disorder (non-equilibrium) as complemented by elastic and quasielastic neutron scatterings. DFT calculations with different lithium distributions at two different crystallographic sites guide to understand the lattice expansion anomaly. The lattice thermal expansion is modeled using Grüneisen first-order approximation, where the Debye–Einstein–Anharmonicity approach provides the temperature-dependent vibrational energy. The DFT-calculated phonon density of states and bulk modulus help extract the characteristic Debye and Einstein frequencies.



## 1. Introduction

For decades, lithium tungsten bronzes ($Li_xWO_3$) have been known for their composition ($x$) dependent interesting electrical and optical properties.[1] The photochromic behavior of $Li_xWO_3$ was reported to be a function of lithium concentration in the system.[2] As such, many electrochromic devices have been designed such as smart windows,[3,4] where lithium was intercalated into the $WO_3$-matix (greenish) by applying voltage, leading to formation of deep-blue $Li_xWO_3$ bronze. Conversely, the reverse voltage resulted in a bleached state of the parent $WO_3$. Although the host $WO_3$ possesses different crystal structures at given temperatures the intercalation at ambient condition transforms the lower symmetric $WO_3$ into a higher symmetric $Li_xWO_3$ bronze.[5] Three different perovskite-type lithium tungsten bronzes, namely, body-centered cubic ($Im\bar{3} \equiv PTB_{CI}$), primitive cubic ($Pm\bar{3}m \equiv PTB_{CP}$) and primitive tetragonal ($P4/nmm \equiv PTB_T$) are known. The crystal structures and the symmetry relation between $PTB_{CI}$ and $PTB_{CP}$ are reported elsewhere.[6] In the $PTB_{CP}$ phase, lithium locates at the center of a cubo-octahedron with a Li–O distance of 263.2 pm.[7] So far known from the updated literatures, the lithium position was not either determined or documented in the $PTB_T$ system. For a hypothetical Wyckoff position of 2*a* (3/4,1/4,0) lying in the channel of $PTB_T$[6] lithium can be viewed at the centroid of a cubo-octahedron with slightly a different Li–O distances, for instance, 261 pm and 266 pm.[8] The $PTB_{CI}$ structure can be described by doubling (372.65 pm × 2 = 745.3 pm) the cell parameter of $PTB_{CP}$,[8] where the $WO_6$ octahedra are tilted about 13° from the cubic axis, however, leaving the tungsten framework undistorted. Fig. 1 shows a representative $PTB_{CI}$ symmetry for the crystal structure of $Li_{0.4}WO_3$. This cooperative rotation leads to three different W–O bond distances as well as two different types of cavities (six centers at 6*b* and another two at 2*a*). As a structural consequences, the host-oxygen displaces about 45 pm from the hypothetical undistorted geometry ($PTB_{CP}$).

From the neutron diffraction data Wiseman and Dickens[7] determined lithium position in the $PTB_{CI}$ system, locating both in the 6*b* and 2*a* sites with a random distribution. Residing at 2*a* site lithium possesses Li–O distances of about 265 pm a closer value to that in the $PTB_{CP}$ and $PTB_T$ phases. On the other

[a] *Univeristy of Bremen, Institute of Inorganic Chemistry and Crystallography, Leobener Straße 7, D-28359 Bremen, Germany. E-mail: murshed@uni-bremen.de; Tel: +49 (0)421 218 63144*
[b] *University of Bremen, Crystallography, Faculty of Geosciences, Klagenfurter Straße 2-4, D-28359 Bremen, Germany*
[c] *Institut Laue Langevin, 38042 GRENOBLE Cedex 9, France*
[d] *Univeristy of Bremen, MAPEX Center for Materials and Processes, Bibliothekstraße 1, D-28359 Bremen, Germany*

† Electronic supplementary information (ESI) available. See DOI: https://doi.org/10.1039/d4cp00752b

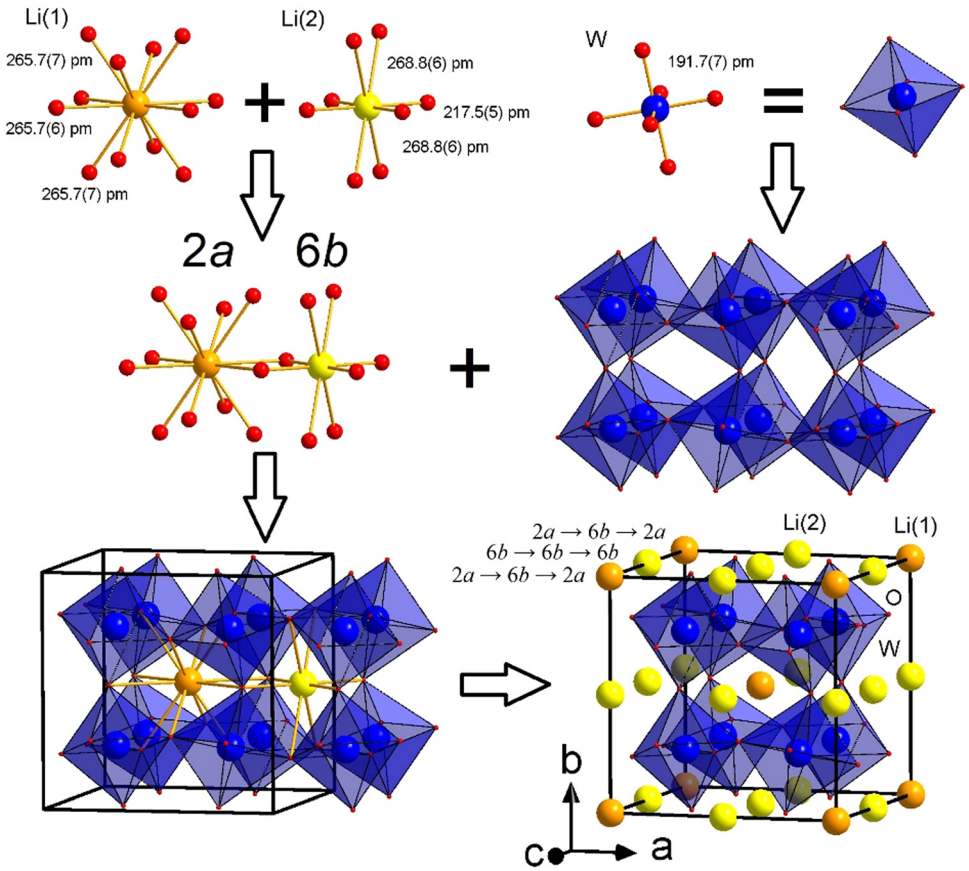


Fig. 1 Crystal structure of $Li_{0.4}WO_3$ bronze, showing two distinct Wyckoff sites (2*a* and 6*b*) and $LiO_x$ coordination. The arrows depict lithium possible pathways from one site to other during diffusion.

hand, sitting in 6*b* site lithium locates at the centroid of a highly distorted cubo-octahedron with strikingly different Li–O distances of 217 pm (4×), 269 pm (4×) and 309 pm (4×).[9] Employing difference Fourier synthesis on neutron powder diffraction (NPD) data Cava *et al.*[9] found lithium only at the 6*b* position, which was later supported by Rahman *et al.*[8] For the last more or less seven decades, a hefty number of studies were reported on $Li_xWO_3$ bronzes. However, temperature-dependent in-depth structural studies on $Li_xWO_3$ are not explored to explain some observed anomalies. For instance, the temperature-dependent heat capacity ($C_p$) showed $\lambda$-type heat capacity anomalies at around 330 K and 460 K for all three $Li_{0.363}WO_3$, $Li_{0.437}WO_3$ and $Li_{0.478}WO_3$ bronzes.[10] $Li_{0.363}WO_3$ exhibited an additional anomaly at much higher temperature of 590 K, which however, was not exhibited by the other two phases.[11] Such heat capacity anomaly could not be explained in terms of displacive phase transition as the space group (symmetry) did not change below and above those critical temperatures. Shanks *et al.*[11] also observed electrical resistivity anomaly at 320 K for $Li_{0.345}WO_3$ without the change of symmetry before and after the heating. Inaba *et al.*[12] showed that the electrical resistivity sharply drop down at about 600 K for $Li_{0.28}WO_3$ followed by a minimum at about 700 K with a further linear increase. $Li_{0.34}WO_3$ exhibits, however, a slight decrease of resistivity at about 300 K followed by broad plateau minimum at about 500 K with slightly a non-linear increase afterward.[12] Comparing these two compositions ($x$), the lithium concentration determines both the value and the drop-down behaviors of the electrical resistivity, whereas the crystal structures are still cubic below and above the critical temperatures.[12] Temperatures (330 K and 600 K) at which the electrical resistivity drops down are consistent to the heat capacity anomalies (320 K and 590 K) in $Li_{0.363}WO_3$. However, a clear-cut explanation for those anomalies is not still available. The present study reports on temperature-dependent behaviors of $Li_{0.4}WO_3$ using elastic and quasi-elastic neutron scatterings, which shed light to explain the thermal anomaly. Density functional theory (DFT) calculation helps guide for the modeling of lattice thermal expansion using Debye–Einstein–Anharmonicity (DEA) model.[12–15]

## 2. Experimental

### 2.1. Synthesis

Polycrystalline powder sample of $Li_{0.4}WO_3$ bronze is synthesized by conventional solid state method using $Li_2WO_4$, $WO_3$ and $WO_2$. Stoichiometric amounts of the starting materials were mixed in an agate mortar and transferred into an annealed quartz tube. The internal air pressure of the quartz

 

tubes was reduced to $10^{-7}$ MPa. The sealed tubes were heated in a muffle furnace at 973 K for seven days. Afterward, the samples were quenched to room-temperature.

### 2.2. Powder X-ray diffraction

The powder X-ray diffraction (XRD) data were collected on a Bruker D8 Advance powder diffractometer equipped with a germanium (111) monochromator and CuK$\alpha_1$ radiation ($\lambda$ = 154.0596 pm). Room-temperature data were recorded using Debye–Scherrer geometry with glass capillaries of 0.3 mm outer diameter. Low-temperature powder X-ray diffraction data were collected on a Rigaku powder diffractometer using Debye–Scherrer geometry. Samples were filled into glass capillaries of 0.2 mm outer diameter. Data were recorded from 100 K to 300 K with 15 K steps and 2$\theta$ range of 5° to 90° with a step width of 0.02°. Temperature-dependent powder X-ray diffraction data were also collected on a Panalytical MPD powder diffractometer with an attached Anton Paar HTK1200N heating chamber. Samples were prepared in a flat corundum sample holder using acetone to submerge the fine powder producing small evaporation channels which served for additional space for the thermal expansion of the compound. Measurements were carried out from 300 K to 780 K with 10 K steps and 2$\theta$ range of 10° to 110° with a step size of 0.0167° and a 40 s per step total data collection time. X-ray powder data Rietveld refinements were carried out using "Diffrac$^{Plus}$ Topas 4.2" software (Bruker AXS GmbH, Karlsruhe). To describe the X-ray diffraction profile the fundamental parameter approach was applied in the Rietveld refinements. For each diffractometer configuration, the corresponding fundamental parameters were fitted to powder data of standard $LaB_6$. During the refinements, general parameters such as scale factors, background parameters (Chebychev polynomial) and average crystallite size were optimized. Additionally, the cell parameters, atomic coordinates and isotropic atomic displacement parameters were refined.

### 2.3. Neutron powder diffraction

Temperature-dependent neutron powder diffraction data (NPD) of $Li_{0.1}WO_3$ and $Li_{0.4}WO_3$ bronzes were recorded using time-of-flight (TOF) neutron flux of POWGEN diffractometer at the Spallation Neutron Source (SNS) (Oak Ridge National Laboratory, USA). The low-temperature data were measured using the Cryo-furnace Janis between 10 K and 300 K with a central wavelength of about 133(1) pm. For the high-temperature NPD, about 4 g of the powder sample was loaded into a thin-walled vanadium sample container followed by placing it into an ILL-type low-pressure ($\sim 2.7 \times 10^{-9}$ MPa) furnace and heated at 380 K to 780 K with a ramping temperature slice of 25 K. The data were collected using a center wavelength of 133.3 pm. The Rietveld refinements were performed using the GSAS suite with EXPGUI interface.[16] A representative NPD data Rietveld plots of $Li_{0.4}WO_3$ is shown in Fig. 2. During the Rietveld refinement the scale factor, absorption coefficient, lattice parameters, fractional coordinates and mean atomic displacement of the atoms were refined. The thermal expansion of $Li_{0.4}WO_3$ bronzes is studied using composite data sets

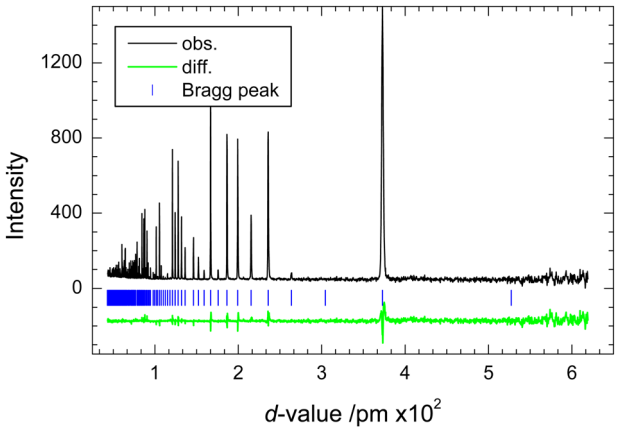


Fig. 2 Representative neutron powder data Rietveld plot of $Li_{0.4}WO_3$ bronze at 300 K.

of PXRD (100–400 K) and NPD (10–300 K and 380–780 K). A linear correction factor of less than one picometer is applied between the PXRD and NPD data at 380 K for the *a*-lattice parameter.

### 2.4. Quasi-elastic neutron scattering (QENS)

QENS spectra were collected on IN6-Sharp@ILL, Grenoble using the cold neutron wavelength of 512 pm with an elastic energy resolution of 70 μeV. The room temperature (295 K) spectrum was taken followed by heating the sample in the quartz tube (synthesis condition) and measured at 563 K and 894 K. Spectra at 471 K and 361 K were also measured while cooling the sample. An empty quartz tube was measured for background. QENS data were collected on the vanadium sample holder, which is entirely an incoherent scatterer. This background data was used for intensity normalization, elastic energy resolution and removal for sample environment.

### 2.5. DFT calculation

Ordered models of $Li_xW_8O_{24}$ for $x$ = 2, 3, 4, 5 and 6 in the conventional cubic unit cell are generated using the supercell code.[17] Different distributions of Li at 2*a* and 6*b* sites are considered. For example, for the $Li_3W_8O_{24}$ stoichiometry, four models are generated for a 3 : 0 6*b* : 2*a* distribution of Li, five models for a 2 : 1 6*b* : 2*a* distribution, and one model for a 1 : 2 6*b* : 2*a* distribution. The structures of all ordered models are then optimized using the CASTEP code.[18] During these optimizations, the atomic coordinates are allowed to change, whereas the relaxation of the cell parameters is constrained to a cubic metric irrespective to the actual symmetry. The CASTEP calculations use the PBEsol exchange–correlation functional[19] employing on-the-fly generated ultrasoft pseudopotentials and a plane-wave cutoff energy of 700 eV. The first Brillouin zone is sampled using a 4 × 4 × 4 mesh of *k*-points. Of notes, the convergence is ensured through additional calculations for $Li_8W_8O_{24}$ using a 8 × 8 × 8 mesh. A DFT-based prediction of the bulk modulus and phonon density of states (PDOS) is carried out for a chosen model of $Li_3W_8O_{24}$ (3 : 0 6*b* : 2*a* distribution of Li, symmetry $Pm\bar{3}$) that lies close to the

experimental composition of $Li_{3.2}W_8O_{24}$. A series of optimizations are carried out for the calculation of bulk modulus using a fixed unit cell size varying from 740 to 750 pm in a step of 2 pm. The bulk modulus is then computed with the 3rd-order Birch–Murnaghan equation of state using the EosFit7-GUI code.[20] The phonon calculation is performed in the framework of the finite-displacement method[21] employing a 2 × 2 × 2 supercell of the conventional unit cell. The PDOS and partial PDOS of the constituent atoms are visualized using a Gaussian broadening of 3.34 $cm^{-1}$, where the integral of the PDOS is set to unity.

## 3. Results and discussion

Both PXRD and NPD data Rietveld refinements confirmed $Li_{0.4}WO_3$ bronze crystallized in the space group $Im\bar{3}$. The crystal structural data of $Li_{0.4}WO_3$ is listed in Table 1, and selected bond distance and angles in Table 2.

Simultaneous refinement of the isotropic atomic displacement parameter (ADP) and occupancy of Li(1) and Li(2) converges unphysical parameters, in particular, of the Li(1) atom may due to lower occupancy of the 2*a* site within the estimated uncertainty. This can be also understood in terms of dimensions of the cavities and the associated large coordination of lithium (Fig. 1). As such, the occupancy between Li(1) and Li(2) are constrained to each other. Repeated trials suggest to set the ADPs of Li(1) to be four times higher than that of Li(2). At low temperatures, for instance at 10 K, the NPD data converges lithium to be mostly located at 6*b* site (51(2)%) and the rest at 2*a* site (7(2)%) (Table 1). Such low-content most probably did not allow to detect light lithium atom at the 2*a* site[6,10] even using NPD. In increasing temperature above 300 K, lithium at 6*b* site decreases and at 2*a* site increases, as shown in Fig. 3. That is, $Li^+$ cation successively moves from 6*b* to 2*a* site within the investigated high temperature elastic neutron scattering between 380 K and 773 K.

For lithium at 6*b* site, four planar oxygen atoms construct an aperture (1/2[shortest O–O distance – $2^{\bullet}r_O$]) of 26.7 pm for Li(2) compared to 39.5 pm for Li(1) formed for the lithium at 2*a* site with twelve-coordinated ($LiO_{12}$) oxygen environment, where $r_O$ refers to cationic radius within the first coordination shell. It seems that kinetically favored the compacted lithium at 6*b* moves to spacious 2*a* site with increasing temperature. The crystal symmetry suggests that once lithium locates at 2*a*, it cannot move to another 2*a* without passing through the 6*b* site (Fig. 1). As such, two diffusion mechanisms (6*b* → 6*b* and 2*a* → 6*b* → 2*a*) were proposed[22] within the Li–Li distance of about 372 pm (Table 2). Therefore, the initial steep increase of lithium at the 2*a* site most probably indicates 6*b* → 2*a* diffusion (Fig. 3). Indeed, due to unavailability of the NPD elastic data we could not follow the lithium occupancy (diffusion) between 300 K and 380 K. This observation can be correlated to the anomaly of electrical resistivity of $Li_{0.345}WO_3$[11] and heat capacity of $Li_{0.363}WO_3$[12] bronzes at high-temperatures. The change of oxygen coordination and the associated tilting of the $WO_6$ octrahedral can be seen in Fig. S1 and S2 (ESI†).

For more in-depth details, the QENS experiment demonstrates lithium diffusive motions by broadening the elastic scattering profile as a function of momentum transfer. The temperature-dependent dynamic structure factors $S(Q,\omega)$ are seen in Fig. 4, showing the superposition of neutron elastic and quasi-elastic scattering components within the accessible *Q*-range between 0.42 and 2.42 $Å^{-1}$. At higher temperatures, the elastic contribution is predominantly visible, in particular at higher *Q*-range. The rapid drop of the elastic intensity up to 470 K, as shown in Fig. S3 (ESI†), indicates a redistribution of the scattering intensity between the elastic and the quasielastic signals. Afterward, both the elastic and the quasielastic intensity remain almost unchanged. Below 470 K the broadening of

Table 1 Crystal structural data of $Li_{0.4}WO_3$ bronze at 10 K obtained from time-of-flight neutron powder diffraction data Rietveld refinement

Space group: $Im\bar{3}$, $a$ = 744.528(2) pm, $V$ = 412.709(3) × $10^6$ $pm^3$, $Z$ = 8, $R_{wp}$ = 4.8%

| Atom | Wyckoff | $x$ | $y$ | $Z$ | Occupancy | $U_{iso}/10^4$ $pm^2$ |
|---|---|---|---|---|---|---|
| Li1 | 2*a* | 0 | 0 | 0 | 0.07(2) | 0.064(3)[a] |
| Li2 | 6*b* | 1/2 | 0 | 0 | 0.51(2) | 0.016(1) |
| W | 8*c* | 1/4 | 1/4 | 1/4 | 1 | 0.0023(3) |
| O | 24*g* | 0 | 0.20399(9) | 0.29127(9) | 1 | 0.0051(1) |

[a] Values are constrained to four times that of Li(2) during the refinement.

Table 2 Selected interatomic distances (/pm) and angles (/°) of $Li_{0.4}WO_3$ bronze at different temperature obtained from time-of-flight neutron powder diffraction data Rietveld refinement

| Bond length/angle | @10 K | @300 K | @773 K |
|---|---|---|---|
| Li(1)–O × 12 | 264.74(6) | 269.69(1) | 266.94(1) |
| Li(2)–O × 4 | 217.28(7) | 218.76(1) | 224.10(1) |
| Li(2)–O × 4 | 269.67(4) | 269.68(1) | 269.51(1) |
| Li(2)–O × 4 | 309.18(5) | 308.55(1) | 306.06(1) |
| W–O × 6 | 191.73(3) | 191.76(1) | 191.87(1) |
| Li(1)–Li(2) | 372.25(1) | 372.83(1) | 374.88(1) |
| W–O–W | 152.23(1) | 152.87(1) | 155.33(2) |

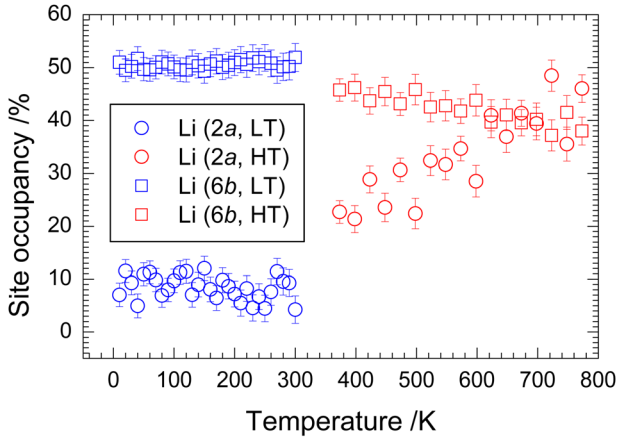


Fig. 3 Temperature-dependent lithium site occupancy in $Li_{0.4}WO_3$ bronze obtained from neutron powder diffraction data Rietveld refinement.

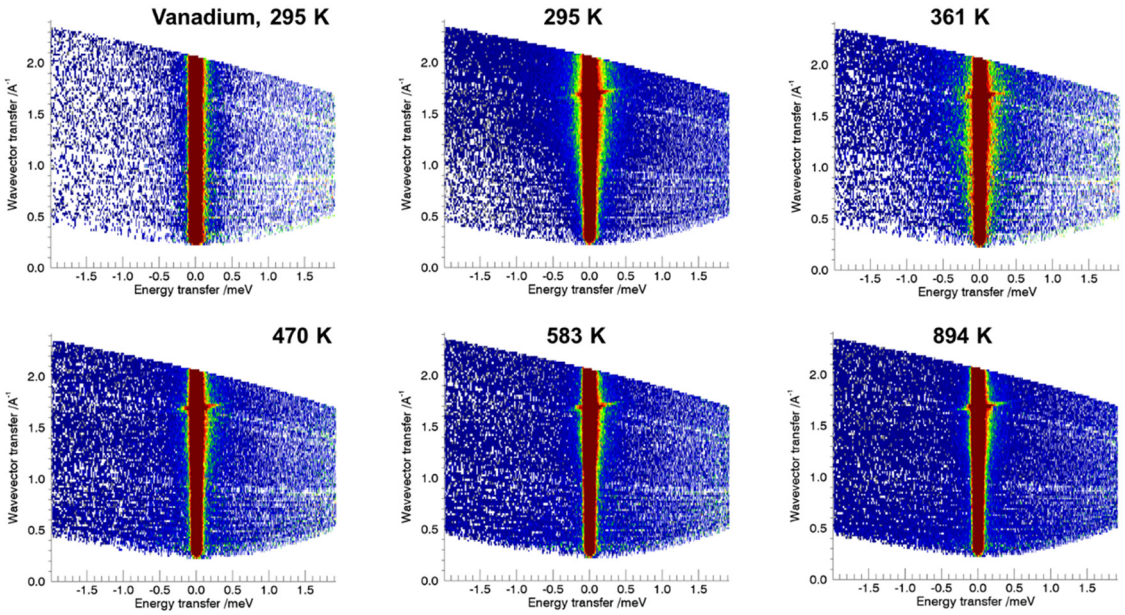


Fig. 4 Temperature-dependent dynamic structure factor $S(Q,\omega)$ of $Li_{0.4}WO_3$ bronze, showing superposition of neutron elastic and quasi-elastic scattering components. Scattering from an empty vanadium can (vana) at ambient temperature is also depicted.

the QENS signal at lower $Q$-range $<1.5$ Å$^{-1}$ is characteristic of jump diffusion.[23] As such, the QENS data analysis is limited to lower temperature range between 295 K and 361 K. The QENS signal is modeled using the expression:

$$S(Q,E) = \left[x\delta(E) + (1-x)\frac{1}{\pi}\frac{\Lambda(Q)}{E^2+\Lambda(Q)^2}\right] \otimes R(E) + B(E) \quad (1)$$

which is a combination of elastic ($\delta(E)$) and quasielastic components (Lorentzian) convoluted with the instrument resolution function $R(E)$ plus the linear background term $B(E)$. $\Lambda(Q)$ refers to half-width-at-half-maximum (HWHM) of the Lorentzian function. Fig. 5 depicts a representative QENS-fit at 361 K for $Q$ = 1.03 Å$^{-1}$. The elastic contribution is partly caused by an incomplete suppression of the high Bragg intensity, which is easily discernible at higher temperatures where the QENS lines are broad enough to differ notably from the elastic scattering. The intensity and the broadening of $S(Q,\omega)$ are analyzed at eight different $Q$-values from 0.39 Å$^{-1}$ to 1.8 Å$^{-1}$ with an incremental slice of 0.16 Å$^{-1}$ to better distinguish between the elastic and quasielastic contributions. However, data analysis is limited to low-$Q$ and low temperature. Fig. S4 (ESI†) shows temperature-dependent QENS signals strongly suppressed by the elastic intensity for $Q > 1.35$ Å$^{-1}$ as the summed $S(Q)$ over all accessible energy of $S(Q,E)$ clearly hints for strong Bragg peaks (Fig. S5, ESI†).

The $Q$-dependency of the HWHM of the Lorentzian component is shown in Fig. 6, showing the observed data up to $Q^2 \sim 2.1$ Å$^{-2}$ ($Q \sim 1.45$ Å$^{-1}$) along with the jump-diffusion model:[23]

$$\Lambda(Q) = \frac{h}{\tau}\left(1 - e^{-D\tau Q^2}\right) \quad (2)$$

where $D$ is the diffusion coefficient and τ the time between the successive jumps. The diffusion coefficient is found to be

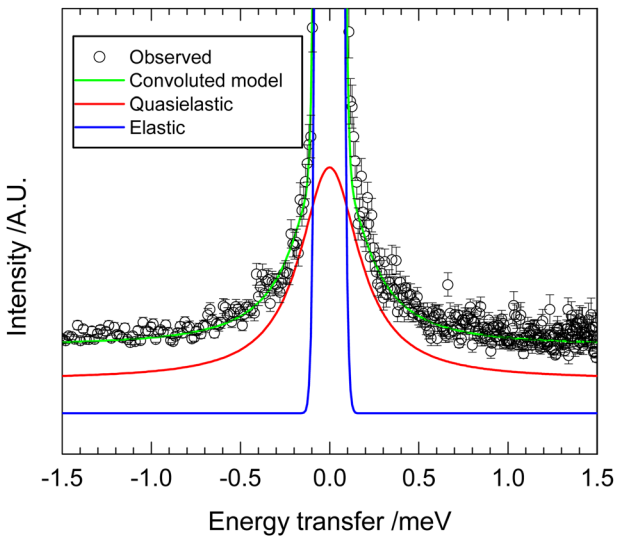


Fig. 5 Representative model fitting using delta- and Lorentzian function for the elastic and the quasielastic contributions of the QENS data at $Q$ = 1.03 Å$^{-1}$ and 361 K.

43(7) × 10$^{-10}$ m$^2$ s$^{-1}$ at 295 K, which increases to 76(5) × 10$^{-10}$ m$^2$ s$^{-1}$ at 361 K. These observed diffusion coefficient values are higher than those of reported ones for lithium diffusion in the $Li_xWO_3$ films[24,25] and in the $WO_3$-matrix[26] as well. The isotropic jump period of 1.4(2) ps and 0.6(1) ps are estimated at 295 K and 316 K, respectively, leading to the jump length ($L$ = sqrt(6 × $D$ × τ)) of 187(5) pm and 170(3) pm, both of which are about half of the Li–Li distance in the $Li_{0.4}WO_3$ bronze (Table 2). The half-length can be explained in terms of the theoretical prediction of the composition-dependent

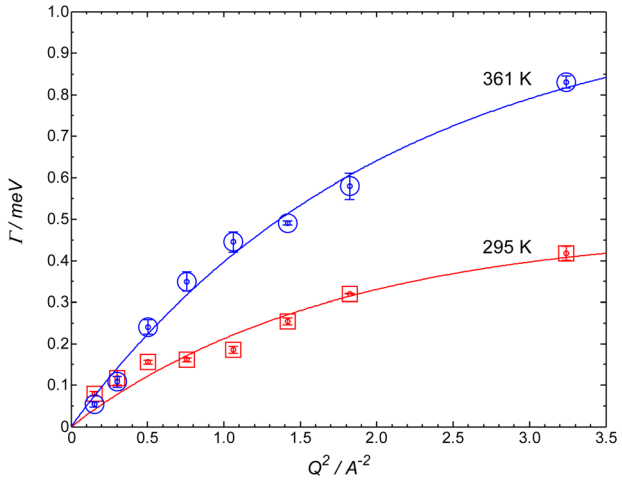


Fig. 6 $Q$-dependence of the half-width at half-maximum ($\Gamma$) of the quasielastic neutron scattering signal of $Li_{0.4}WO_3$ bronze at two different temperatures. The solid lines refer to model (eqn (2)) that does consider data points $Q^2 > 2.0$ Å$^{-2}$.

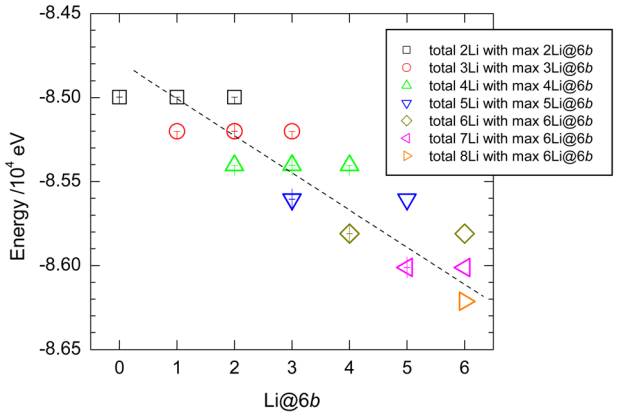


Fig. 7 DFT calculated total energy as function of lithium at the 6*b* site of the $Li_xW_8O_{24}$ bronze. The uncertainty refers to energy difference with respect to the lowest-energy model for a given composition.

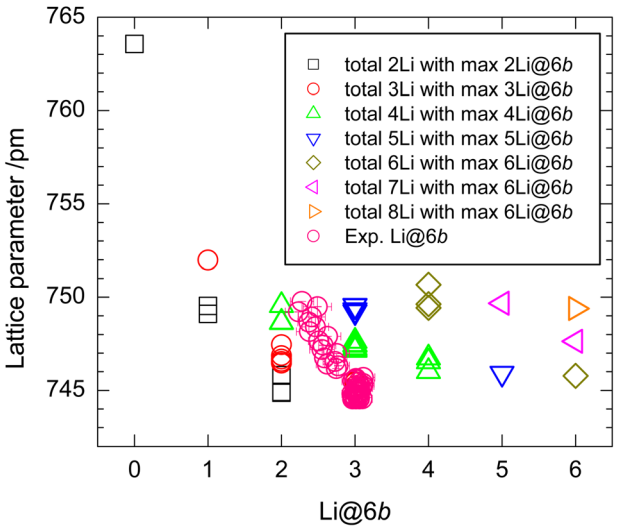


Fig. 8 DFT calculated lattice parameter as function of lithium at the 6*b* site of the $Li_xW_8O_{24}$ bronze.

potential barrier for the diffusion of lithium in the cubic $Li_xWO_3$ systems,[27] where the diffusion barrier height is limited to $x < 0.3$, and $x = 0.4$ indicates one of the highest potential barriers. As such, at higher temperatures the chance for lithium diffusion seems to be less, resulting in limited lithium dynamics between 2*a* and 6*b* sites without a net translation. Evidently, at temperatures >361 K the Lorentzian of the HWHM becomes narrower (Fig. S5, ESI†).

During DFT optimization of the models with different total Li-content, various lithium distributions between 6*b* and 2*a* sites result in two cubic ($Im\bar{3}$, $Pm\bar{3}$) and two pseudo-cubic (*Pmmm, Immm*) space groups, as listed in Table S1 (ESI†). For all Li-contents considered, the lowest-energy model corresponds to a model where the 6*b* site keeps a maximal occupancy, as shown in Fig. 7. This findings agree well with the experimental observation that the 6*b* site is predominantly occupied at low temperatures. It is also noteworthy that some models, where the 2*a* site is partially or fully occupied, stabilize with a typical energy difference of a few kJ mol$^{-1}$. It could thus be expected that this site is occupied to an increasing extent with increasing temperature. On the other hand, irrespective to the space groups evolution of the lattice parameter suggests to be a function of distributive lithium content at the 6*b* site, as shown in Fig. 8. With increasing lithium at the 6*b* site the lattice parameter sharply decreases for low-content lithium followed by broad fluctuation around an average value of 745.5 pm. Ignoring the thermal expansion the experimental NPD data lattice parameters lie within this broad range (±5 pm). On the other hand, keeping lithium only at the 6*b* site (2*a* completely vacant), the lattice parameters show a critical high value for 4 lithium at the 6*b* site, as seen from Fig. S6 (ESI†). That is, lithium content less than 3 at the 6*b* site experiences a lattice contraction.

Temperature-dependent isotropic atomic displacement parameters (ADPs) are shown in Fig. 9 along with the Debye-fit model suggested by Lonsdale.[28] The ADPs agree well with the common findings of higher values for lighter elements in the order Li > O > W. The static disorder, calculated from the 0 K intercept of the extrapolation of the ADPs down to the Debye temperature, agrees well with the values calculated from the direct Debye-fit of the temperature-dependent ADPs which monotonically increases over the whole temperature range. The atom-weighted Debye temperature is estimated to be 522(15) K. While the ADPs of oxygen and tungsten atoms lie on the model-line for the investigated temperature range, the lithium ADP departs above 373 K. The departure with successive lower ADPs indicates a certain degree of interactions with the framework oxygen may due to potential barrier. This assumption is supported by the QENS results.

Temperature-dependent evolution of cell volume and thermal expansion coefficient (TEC) of $Li_{0.4}WO_3$ bronze is shown in Fig. 10. A sharp kink of TEC starts at about 410 K, which

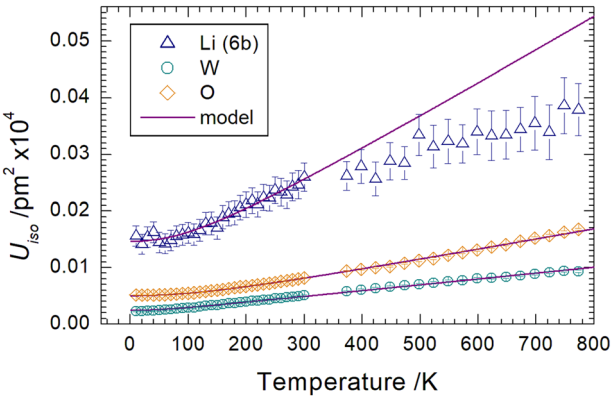


Fig. 9 Temperature-dependent isotropic displacement parameters (ADPs) of the constituent atoms in $Li_{0.4}WO_3$ bronze obtained from neutron powder diffraction data Rietveld refinements.

however, resumes to the usual increasing trend above 500 K. Careful neutron elastic data analysis does not hint for displacive phase transition. The lattice thermal expansion has been tested using Grüneisen first-order approximation, where the temperature-dependent vibrational energy is calculated using the DEA model.[12–15] Alike other bronzes,[29] considering lithium as an Einstein rotor inside the $WO_3$-matrix, the Debye–Einstein approach which is a representative fragment of the DEA model,[12–15] could not appear with physically meaningful convergence. Using even an additional isochoric anharmonicity term could not model the mid-range sharp anomaly. The phonon density of states (PDOS), however, guides for the modeling of the lattice thermal expansion. Fig. S7 (ESI†) depicts the PDOS of $Li_3W_8O_{24}$ along with the constituent contributions, where all the lithium atoms are located only at 6*b* of the space group $Pm\bar{3}$. The PDOS shows two continua (0–480 cm$^{-1}$ and 480–990 cm$^{-1}$) with a noticeable phononic band gap of 70 cm$^{-1}$ between 480 cm$^{-1}$ and 550 cm$^{-1}$. From the atomic PDOS it is clear that the low-frequency continuum is contributed by all the atoms and the high-frequency continuum is composed of the framework oxygen only. Of particular notes, even as a light element the lithium does not contribute to the high-frequency continuum. Moreover, it's wide-extended contribution to the low-frequency region distinguishes lithium from other heavier atoms[29] in the bronze channels acting as an Einstein rotor inside the $WO_3$-matrix. The thermal expansion modeling considers two separate temperature regions of low- (LT; 10–400 K) and high-temperature (HT; 410–773 K). These two models show a crossover at 410 K, where the TEC anomaly exhibits the deep minimum (Fig. 10), supporting the heat capacity[10] and electrical resistivity[11] anomalies for $Li_xWO_3$ bronzes. Using only single Debye term, the LT-fit shows an excellent convergence, resulting in zero-point cell volume of $412.72 \times 10^6$ pm$^3$ and a Debye temperature of 508(8) K, which lies within the first continuum (353(5) cm$^{-1}$) of the PDOS. Taking 147(3) GPa of the bulk modulus, the thermodynamic Grüneisen parameter is estimated to be 1.3(3) from the fit thermoelastic parameter of $8.82(1) \times 10^{-12}$ Pa$^{-1}$. The HT-data requires one Debye (662(5) K) and one Einstein (1366 K) terms with a thermoelastic parameter of $7.26(2) \times 10^{-12}$ Pa$^{-1}$), leading to a Grüneisen parameter of 1.1(1). Both the Debye cut off at 460(3) cm$^{-1}$ and the Einstein frequency at 950(2) cm$^{-1}$ well represent the PDOS. Modeling the heat capacity ($C_p$)[10] for the composition $Li_{0.4}WO_3$ obtained from the averaged value of reported $Li_{0.363}WO$ and $Li_{0.437}WO_3$,[10] requires only one Debye-term with a characteristic temperature of 645(5) K that lies close to the obtained Debye temperature (662(5) K). The necessity of an additional Einstein temperature for the HT-region suggests HT-oxygen dynamics most probably driven by the lithium

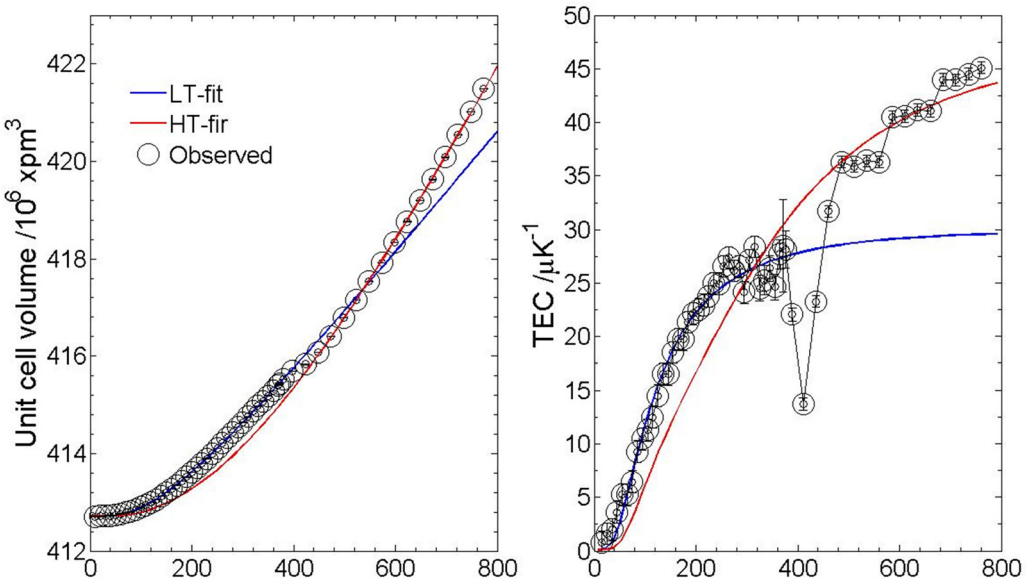


Fig. 10 Temperature-dependent unit cell volume and thermal expansion coefficient (TEC) of $Li_{0.4}WO_3$ bronze along with model fit, where a single Debye term is used for the low-temperature (LT) and a Debye–Einstein model is used for the high-temperature (HT) data set.

dynamics, which however cannot be explained from the PDOS at 0 K. Margaret *et al.*[30] explained lattice expansion with increasing compositional $x$ for $Na_xWO_3$, $Gd_xWO_3$ and $U_xWO_3$ bronzes in terms of structural valence of tungsten cation ($W^{6+}$ to $W^{5+}$) and $WO_6$ octahedral tilting. In contrast, the $Li_xWO_3$ bronze significantly contracts with increasing $x$-content due to $Li^+$ delocalization over the $WO_3$ framework matrix. As a consequence, the Li–O interaction increases, leading to $WO_6$ octahedral tilting. For instance, the tilt is about 14° for $Li_xWO_3$, and 4° for $Na_xWO_3$ and zero degree for $LaWO_3$.[22] Our DFT calculation also supports that in increasing lithium content in particular at the 6*b* site leads to contraction of the lattice parameter (Fig. 8) due to strong Li–$WO_3$-matirx interactions followed by $WO_6$ octahedral tilting. Whereas a sharp maximum of the $WO_6$ octahedral tilting could not be seen at the lattice expansion anomaly region, however, the Li-content at the 2*a* site sharply increases at the temperature regime (Fig. 3). Since lithium translation from 2*a* to 2*a* eventually involves 6*b* site, the dynamic disorder of lithium between these sites at the anomaly region seems to be a non-equilibrium phenomenon. Because, the lattice parameter during electrochemical insertion of lithium into $WO_3$ matrix for the composition $Li_{0.4}WO_3$ clearly deviates before and after the equilibration.[31] Except the anomalous region the overall TEC behavior can be explained by usual lattice dynamics when the lithium occupancy between these two sites does not significantly change.

## 4. Conclusion

Temperature-dependent neutron elastic and quasielastic scatterings allow explaining the thermal expansion anomaly of $Li_{0.4}WO_3$ bronze. DFT calculations suggests that the distribution of lithium at two different crystallographic sites (2*a* and 6*b* in $Im\bar{3}$) play important roles for the lattice parameters. As such, the thermal anomaly has been described as an interplay between lithium dynamics, Li–$WO_3$ matrix interaction and $WO_6$ octahedral tilting. Indeed, such anomaly indicates occurrence of subtle dynamic disorder driven structural metastability (non-equilibrium) within a narrow temperature window. It is reasonable to assume that the higher Li–$WO_3$ matrix interaction at higher temperature kinetically favors the 6*b* site at reaction temperature, which is usually quenched during the sample recovery. As such, it is also assumed that upon slow cooling, the lithium can be found at both sites in $Li_{0.4}WO_3$ bronze.

## Conflicts of interest

There are no conflicts to declare.

## Acknowledgements

We acknowledge University of Bremen for the financial support in perusal of the PhD dissertation of M. S. Rahman who synthesized the sample. MF acknowledges funding by the Deutsche Forschungsgemeinschaft (DFG) through the Heisenberg fellowship number 455871835. We gratefully acknowledge the computing time provided on the supercomputers Lise and Emmy at NHR@ZIB and NHR@Göttingen as part of the NHR (Nationales Hochleistungsrechnen) infrastructure. We thank ILL/Grenoble for providing neutron beam time and supports. Part of the research conducted at ORNL's Spallation Neutron Source was sponsored by the Scientific User Facilities Division, Office of Basic Energy Sciences, US Department of Energy.

## References

1 M. E. Straumanis and S. S. Hsu, The Lithium Tungsten Bronzes, *J. Am. Chem. Soc.*, 1950, **72**(9), 4027–4030.
2 C. G. Granqvist, Electrochromic tungsten oxide films: Review of progress 1993–1998, *Sol. Energy Mater. Sol. Cells*, 2000, **60**(3), 201–262.
3 M. Green, $WO_3$-Based Eleetroehromie Windows Problems and Status., *Ionics*, 1999, **5**, 161–170.
4 Y. Djaoued, S. Balaji and R. Brüning, Electrochromic Devices Based on Porous Tungsten Oxide Thin Films, *J. Nanomater.*, 2012, **2012**, 1–9.
5 Q. Zhong, J. R. Dahn and K. Colbow, Lithium intercalation into $WO_3$ and the phase diagram of $Li_xWO_3$, *Phys. Rev. B: Condens. Matter Mater. Phys.*, 1992, **46**(4), 2554–2560.
6 M. S. Rahman, M. M. Murshed and T. M. Gesing, Synthesis, characterization and time dependent phase transformation of $Li_{0.4}WO_3$ bronze. Zeitschrift für Kristallographie – Crystalline, *Materials*, 2014, **229**(12), 797–805.
7 P. J. Wiseman and P. G. Dickens, Neutron-Diffraction Studies of Cubic Tungsten Bronzes, *J. Solid State Chem.*, 1976, **17**(1–2), 91–100.
8 M. E. Straumanis and G. F. Doctor, The System Sodium Tungsten Bronze Lithium Tungsten Bronze Tungsten(VI) Oxide., *J. Am. Chem. Soc.*, 1951, **73**(7), 3492–3496.
9 R. J. Cava, *et al.*, The Structures of the Lithium Inserted Metal-Oxides Li0.2reo3 and $Li_{0.36}WO_3$, *J. Solid State Chem.*, 1983, **50**(1), 121–128.
10 H. Inaba and K. Naito, Heat-Capacity Measurement of Cubic Lithium Tungsten Bronzes from 200 to 800 K, *J. Solid State Chem.*, 1976, **18**(3), 279–282.
11 H. R. Shanks, P. H. Sidles and G. C. Danielson, Electrical Properties of the Tungsten Bronzes, in *Nonstoichiometric Compounds*, ed. R. Ward, 1963, pp. 237–245.
12 M. M. Murshed and T. M. Gesing, Anisotropic thermal expansion and anharmonic phonon behavior of mullite-type $Bi_2Ga_4O_9$, *Mater. Res. Bull.*, 2013, **48**(9), 3284–3291.
13 M. M. Murshed, *et al.*, Anisotropic lattice thermal expansion of $PbFeBO_4$: A study by X-ray and neutron diffraction, Raman spectroscopy and DFT calculations., *Mater. Res. Bull.*, 2014, **59**, 170–178.
14 M. M. Murshed, *et al.*, Thermal expansion modeling of framework-type $Na[AsW_2O_9]$ and $K[AsW_2O_9]$., *Mater. Res. Bull.*, 2016, **84**, 273–282.
15 M. M. Murshed, *et al.*, Thermal behavior of mullite between 4 K and 1320 K, *J. Am. Ceram. Soc.*, 2017, **100**(11), 5259–5273.

16 B. H. Toby, EXPGUI, a graphical user interface for GSAS, *J. Appl. Crystallogr.*, 2001, **34**, 210–213.
17 K. Okhotnikov, T. Charpentier and S. Cadars, Supercell program: a combinatorial structure-generation approach for the local-level modeling of atomic substitutions and partial occupancies in crystals, *J. Cheminf.*, 2016, **8**, 17.
18 S. J. Clark, *et al.*, First principles methods using CASTE, *Z. Kristallogr.*, 2005, **220**, 567–570.
19 J. P. Perdew, *et al.*, Restoring the density-gradient expansion for exchange in solids and surfaces, *Phys. Rev. Lett.*, 2008, **100**(13), 136406.
20 J. Gonzalez-Platas, *et al.*, EosFit7-GUI: a new graphical user interface for equation of state calculations, analyses and teaching, *J. Appl. Crystallogr.*, 2016, **49**(4), 1377–1382.
21 W. Frank, C. Elsasser and M. Fahnle, Ab initio force-constant method for phonon dispersions in alkali metals, *Phys. Rev. Lett.*, 1995, **74**(10), 1791–1794.
22 A. J. Mark, I. D. Raistrick and R. A. Huggins, The Kinetics of the Electrochemical Insertion of Lithium into Cubic Sodium Tungsten Bronzes, *J. Electrochem. Soc.*, 1983, **130**(4), 776–783.
23 P. L. Hall and D. K. Ross, Incoherent neutron scattering functions for random jump diffusion in bounded and infinite media, *Mol. Phys.*, 1981, **42**(3), 673–682.
24 G. Leftheriotis, S. Papaefthimiou and P. Yianoulis, Dependence of the estimated diffusion coefficient of $Li_xWO_3$ films on the scan rate of cyclic voltammetry experiments, *Solid State Ionics*, 2007, **178**(3–4), 259–263.
25 C. O. Avellaneda and L. O. S. Bulhões, Intercalation in $WO_3$ and $WO_3$:Li films, *Solid State Ionics*, 2003, **165**(1), 59–64.
26 J. García-Cañadas, *et al.*, Charging and diffusional aspects of Li+ insertion in electrochromic a-$WO_3$, *Solid State Ionics*, 2004, **175**(1), 521–525.
27 L. Gracia, *et al.*, Composition Dependence of the Energy Barrier for Lithium Diffusion in Amorphous $WO_3$, *Electrochem. Solid-State Lett.*, 2005, **8**(10), J21.
28 K. Lonsdale, Vibration Amplitudes of Atoms in Cubic Crystals, *Acta Crystallogr.*, 1948, **1**, 142–149.
29 N. J. Chesser, *et al.*, Phonon spectra of hexagonal potassium tungsten bronze ($K_{0,33}WO_3$), *Ferroelectrics*, 1977, **16**(1), 115–118.
30 M. A. Wechter, H. R. Shanks and A. F. Voigt, Relations between lattice parameter and x value for some cubic tungsten bronzes, *Inorg. Chem.*, 1968, **4**, 845–846.
31 K. H. Cheng and M. S. Whittingham, Lithium incorporation in tungsten oxides, *Solid State Ionics*, 1980, **1**, 151–161.